

## Chapter 4

# Integrated model building workflow

Recent increases in computing power have shifted model-building bottlenecks from computational tasks (such as imaging) and toward interpretation and similar human-intensive tasks. One approach to alleviate these bottlenecks is to develop computational interpretation tools, which can allow interpreters to take advantage of increased computational capabilities, while still allowing them to use their expertise to control the interpretation workflow. Two such tools, explored in previous chapters, are seismic image segmentation, and an efficient velocity model-evaluation method using synthesized wavefields. Here, I will use a 3D field data example from the Gulf of Mexico to demonstrate how these two tools can work together to effectively generate and test velocity models based on different salt scenarios. When an improved model is identified, re-migration with the new velocity model leads to an improved subsalt image.

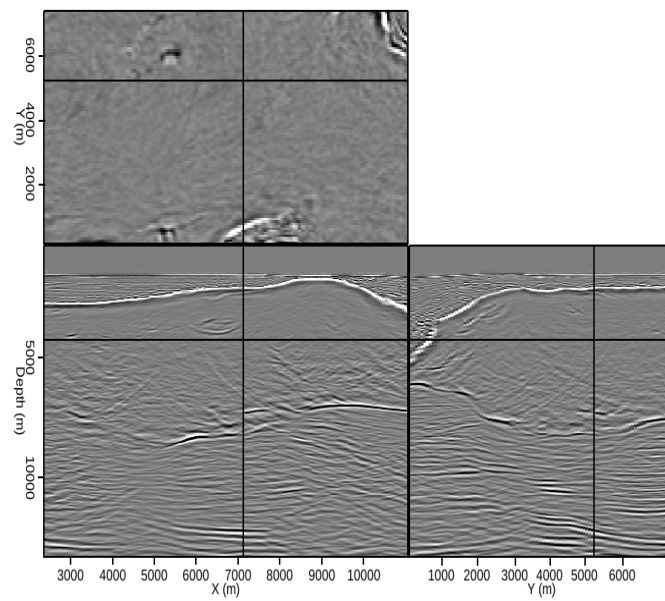
In the following sections, I will briefly review the methods used for both the image segmentation and model evaluation parts of the computational interpretation workflow. I will then demonstrate how these tools can be applied to a 3D example, using

a dataset from a wide-azimuth survey in the Gulf of Mexico, provided by Schlumberger Multicient. The wide-azimuth nature of the survey should allow for sufficient illumination of subsalt areas to image subsalt reflectors, subject to the accuracy of the velocity model. An initial image generated using a velocity model provided with the data can be seen in Figure 4.1(a). Note that a fading of the reflectors directly beneath the salt body suggests possible errors in the velocity model provided with the data (4.1(b)). In particular, note that an inclusion within the salt body has not been assigned a velocity distinct from the rest of the salt, and that the interpretation of the base of salt is somewhat ambiguous. Both of these factors could contribute to the fading of the subsalt reflectors, and are addressed in the creation of the alternate velocity models, which are generated using image segmentation tools. Finally, I will compare the original model and the two alternate models using the synthesized wave-field methodology described in Chapter 3, and validate the comparison by showing a full re-migration of the data using the alternate model judged to be most accurate.

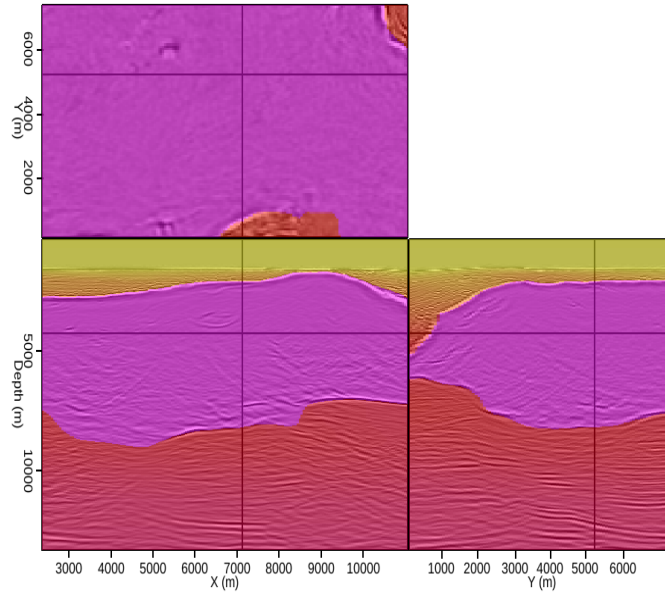
## IMAGE SEGMENTATION

The Pairwise Region Comparison (PRC) image segmentation algorithm is a graph-cut technique based on the method of Felzenszwalb and Huttenlocher (2004). In Chapter 2, I described how this extremely efficient method can be adapted for use with seismic images. Recall that the goal of the example shown here is to improve continuity of the subsalt reflectors in Figure 4.1(a), which is an image obtained using one-way migration and the velocity model in Figure 4.1(b). Based on examination of the velocity model in Figure 4.1(b), two specific areas of possible improvement are the inclusion within the salt body, and the base-salt interpretation. Both of these areas can be addressed separately with image segmentation tools.

Figure 4.2(a) is a close-up image of the salt inclusion mentioned above. By isolating this smaller region for segmentation analysis, we are free to set the minimum segment size to a small number, allowing the automatic segmentation process to capture a higher degree of detail. An additional advantage of this strategy is that the



(a)



(b)

Figure 4.1: (a) A 3D image from the Gulf of Mexico (data courtesy of Schlumberger Multiclient) obtained via one-way migration with the velocity model shown in (b). A prominent sediment inclusion within the salt body, and/or a misinterpreted base of salt, may contribute to the subsalt reflectors' loss of continuity. [CR]

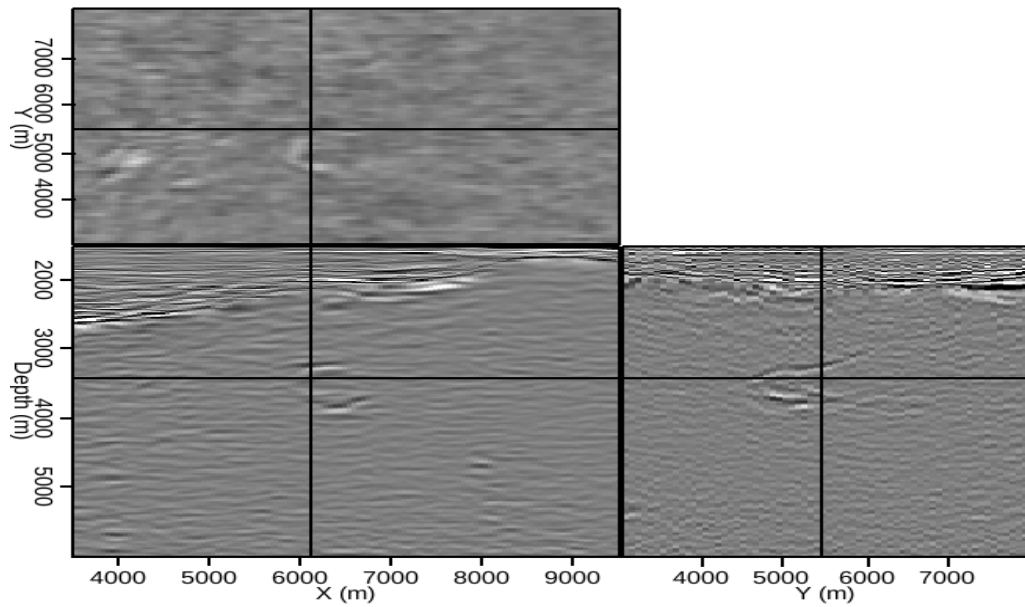
chap4/. img-init,vel-orig

limited domain allows for near-instantaneous segmentations, giving an interpreter the chance to experiment with parameters in an interactive fashion. Figure 4.2(b) is the automatic segmentation result for the salt inclusion. A new base-salt boundary can be defined by again isolating the base-salt region, and performing a detailed segmentation. By choosing which segments to include or exclude from the salt body, any number of possible boundaries can be defined. For this example, I created two different base-salt interpretations, one more aggressive in removing salt than the other. Based on the segmentations of both the salt inclusion and base salt, new velocity models were produced by assigning appropriate sediment velocities to the segmented regions which were originally salt. Figure 4.3 shows the original and two modified velocity models for this region. In this case, replacement velocities were taken at appropriate depths from the background sediment velocities in areas without salt.

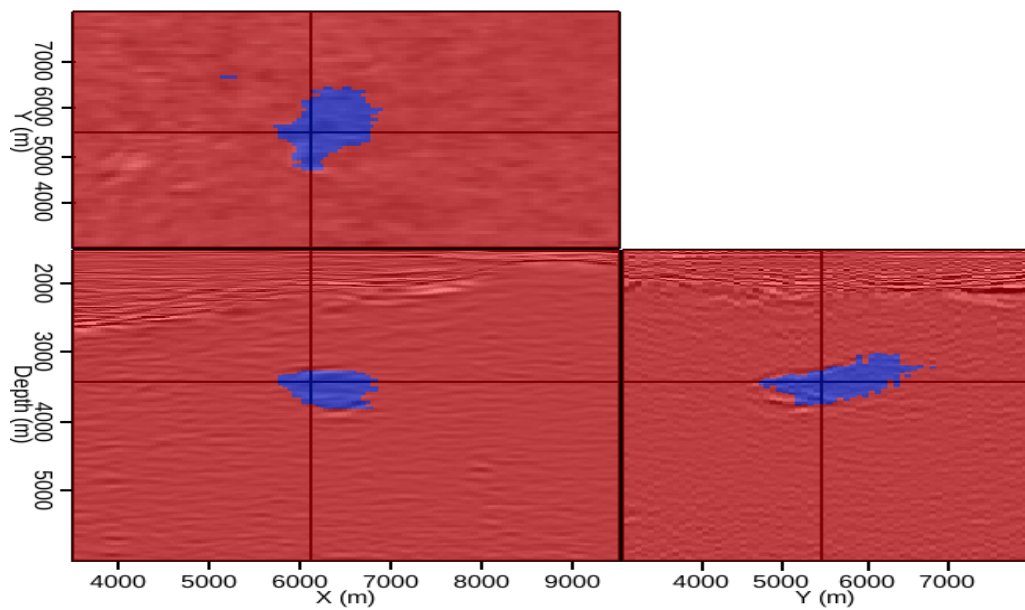
## MODEL EVALUATION

Now, I will test the models created in the previous section using the efficient velocity model evaluation scheme described in Chapter 3. Recall that this method uses an initial image to generate a new areal source function, and then uses this source function to synthesize a new receiver wavefield via Born modeling, again using the initial image as a reflectivity model. Because this receiver wavefield is kinematically invariant of the velocity model used to create the initial image, we can then fairly (and efficiently) test any other models using the synthesized wavefields.

To test the models seen in Figure 4.3, I will investigate the effects of changing the model on a single reflector – in this case, the base salt reflector indicated in Figure 4.4. To do this, I performed several rounds of the evaluation procedure, in an attempt to build a clearer picture of the reflector than if only one or two locations were used in a single experiment. Following the strategy demonstrated in Figure 3.8(c), the image results from each experiment are summed into a final result. According to the procedure outlined above and described in detail in Chapter 3, new areal source and receiver wavefields are synthesized using the initial image and velocity model shown

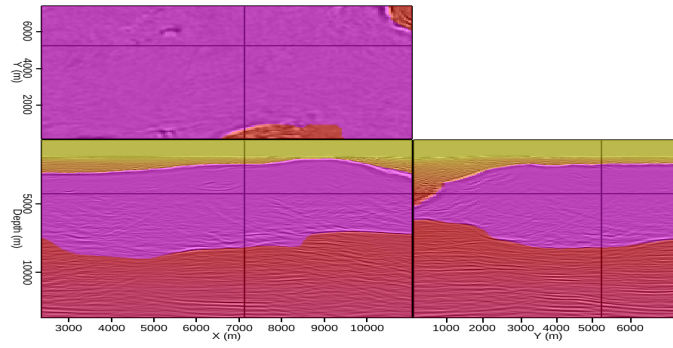


(a)

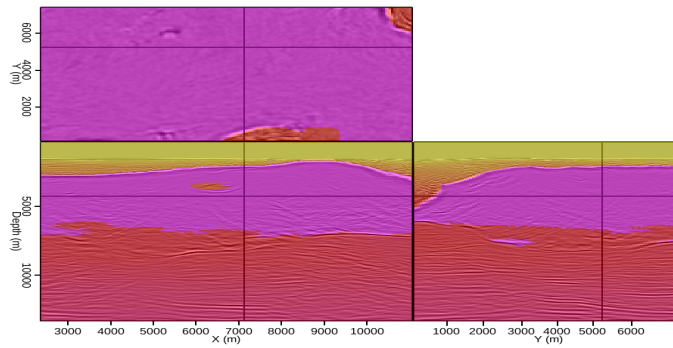


(b)

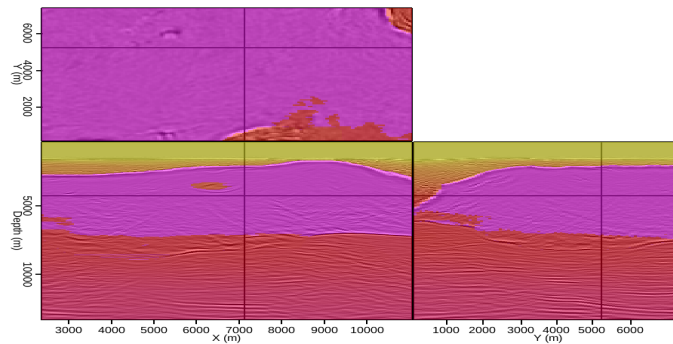
Figure 4.2: (a) Close-up view of the sediment inclusion first seen in Figure 4.1(a); (b) Interpreter-guided 3D segmentation of the image in (a). [CR] chap4/. sizoom-img,sizoom-seg



(a)



(b)



(c)

Figure 4.3: (a) The velocity model provided with the data; (b) An updated model based on the segmentation result in Figure 4.2(b) (and another defining an alternative base-salt interpretation). [CR] chap4/. vzoom-orig1,vzoom-new1,vzoom-new2

in Figure 4.1. Then, isolated locations from the picked reflector are imaged using the three different models in Figure 4.3. The results in Figure 4.5 are qualitatively similar; although differences are apparent due to the changing salt interpretation, it is difficult to make a judgment as to the models' relative accuracy simply using the images at zero subsurface offset. In this situation, information from the subsurface offset domain can be used to detect both qualitative and quantitative differences between the three models.

Qualitatively, we can examine panels displaying subsurface offset data in both the  $x$  and  $y$  directions, at specific  $x, y, z$  locations from the image. The white arrows in each panel of Figure 4.5 indicate equivalent locations along the base-salt reflector, at which the subsurface offset panels in Figure 4.6 were extracted. Figure 4.6(c), extracted from the image migrated with the more conservative alternate velocity model, clearly shows the highest degree of focusing near zero subsurface offset. Because it would be tedious to examine multiple locations along the reflector in this fashion, a quantitative measure of image focusing is desirable. Recall that when using the image focusing measure  $F$  from equation 3.5, a value of  $F = 1$  means that all energy is perfectly focused at zero offset; as  $F$  decreases toward zero the image becomes progressively less focused. Table 4.1 displays the  $F$  value calculations corresponding to each of the images in Figure 4.5. In this case, the  $F$  value for the image obtained using the velocity model with the more conservative removal of salt was the highest. Thus, both the qualitative examination of the subsurface offset panels in Figure 4.6, and the quantitative calculations summarized in Table 4.1, agree that the more conservative alternate model yields the best-focused image.

## RE-MIGRATION

To test the prediction of the model evaluation procedure, full migrations were performed using both the initial model and the alternate model identified in the previous section as the most accurate. One-way, split-step Fourier migration with interpolation

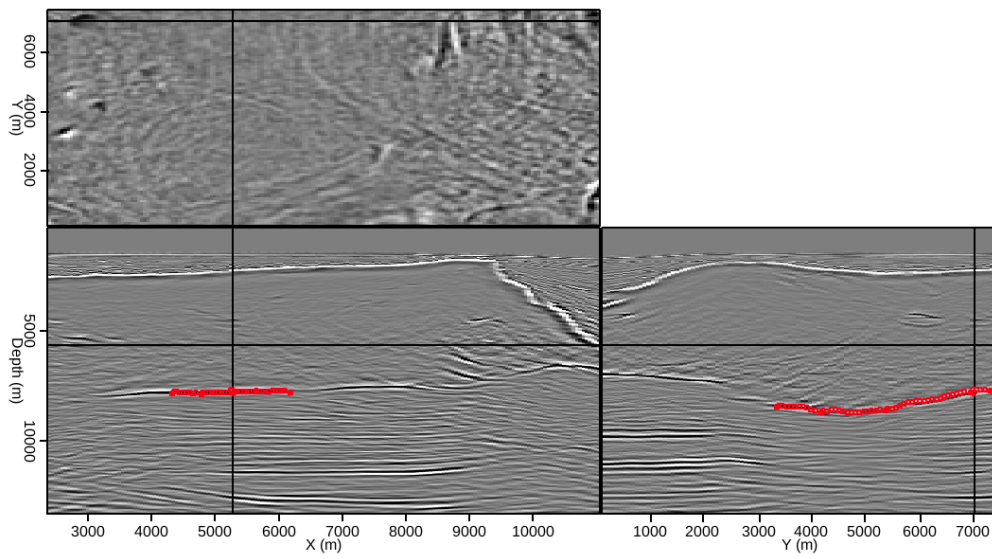


Figure 4.4: A manually-selected base-salt reflector that will be used to quickly evaluate the velocity models in Figure 4.3. [CR] chap4/.img-o2p

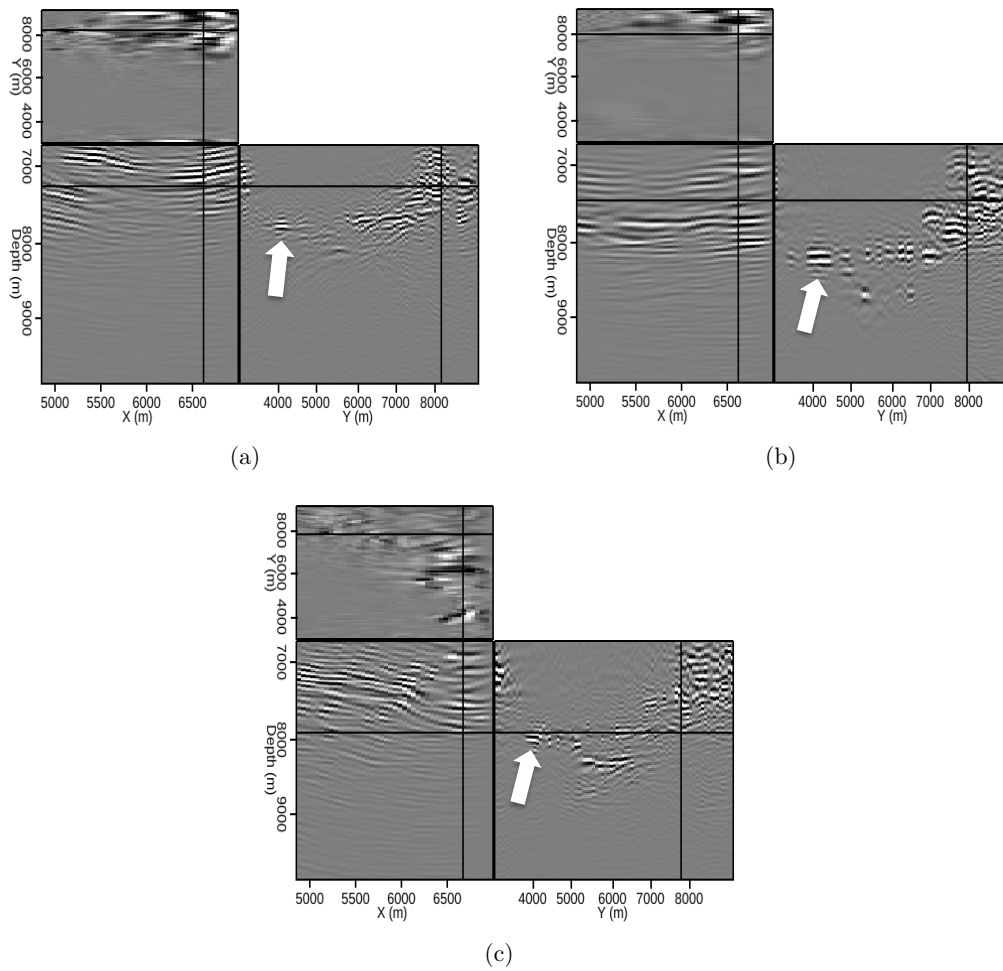


Figure 4.5: Results of performing multiple rounds of the model evaluation procedure on different locations along the reflector indicated in Figure 4.4, and summing the results. The velocity models used for the final imaging step correspond to those in Figure 4.3: (a) the original velocity model; (b) an alternate model with aggressive removal of salt; and (c) an alternate model with more conservative salt removal. The arrows indicate locations at which the subsurface offset panels in Figure 4.6 were extracted. [CR] chap4/. bsum-orig,bsum-v1,bsum-v2

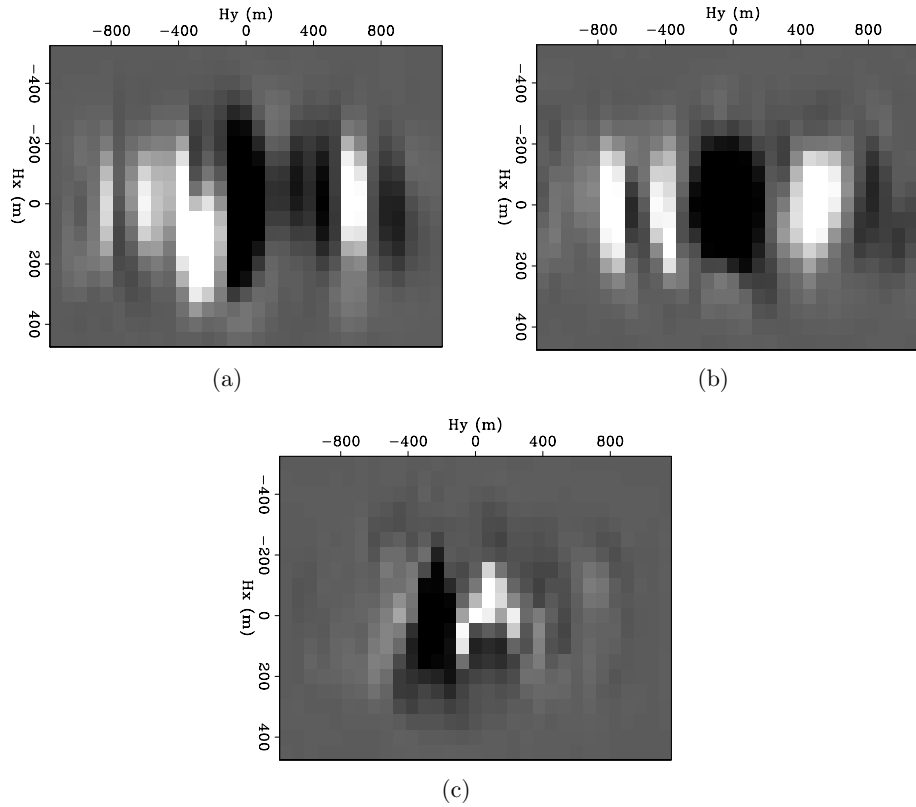


Figure 4.6: Subsurface offset panels at a single  $x, y, z$  location indicated by the arrows in Figure 4.5 for the image corresponding to (a) the original velocity model; and alternate models with (b) aggressive and (c) more conservative removal of salt. The greater degree of focusing near zero subsurface offset in (c) suggests a more accurate velocity model. [CR] chap4/. hxy-orig1,hxy-k4,hxy-k10

Migration model	$F$ value
Initial model	0.785
Aggressive salt removal	0.791
Conservative salt removal	0.810

Table 4.1: Calculations from equation 3.5 for each migration velocity model in Figure 4.3, after the initial image and synthesized wavefields were created using the initial velocity model.

(Stoffa et al., 1990) was used, with five reference velocities selected via Lloyd’s algorithm (Lloyd, 1982; Clapp, 2004). The input data and parameters were identical for both migrations; the only difference was the velocity model. In order to compare the results, I will show both images at two different locations. Figures 4.7(a) and 4.7(b) show images at the first location, produced using the initial and new models, respectively. Figure 4.8 shows the same two images, with areas of particular improvement indicated with arrows and circles. At this location, both the base-salt reflector and the deepest subsalt reflectors show the greatest improvement with the new velocity model. Images from the second location are in Figure 4.9, with annotated versions of the same images seen in Figure 4.10. At this location, the new velocity model yields an image with improved continuity of subsalt reflectors, as well as a more accurate depiction of the salt inclusion itself.

## CONCLUSIONS

Computational interpretation tools such as interpreter-guided image segmentation and efficient model evaluation using synthesized wavefields can effectively add automation to an interpreter-driven model building workflow. In this 3D field data example, image segmentation was used to delineate a salt body inclusion and define two versions of the base of salt different from that of the original model. To test new velocity models derived from these segmentations, several Born-modeled wavefields were synthesized and used to quickly image isolated locations from the base-salt reflector. When summed, the results of these experiments provided a more complete view of the reflector than would be possible using only sparse locations from a single experiment. Qualitative and quantitative analysis of the results suggested that a new model with conservative removal of salt would produce a better-focused image, and full migrations using both the initial model and this updated model confirmed that the new model produced improved continuity in both the base of salt and subsalt reflectors.

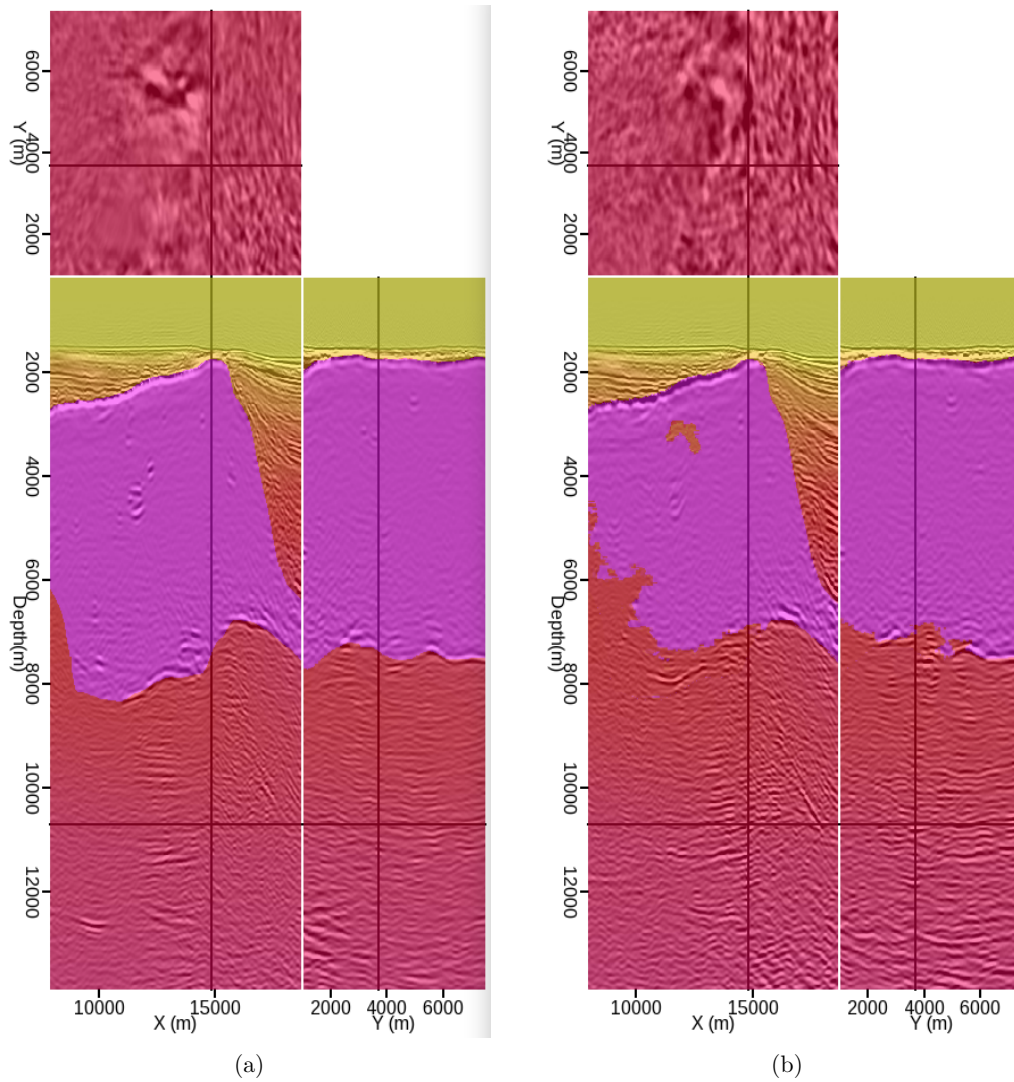


Figure 4.7: Full, one-way migrations with identical parameters using (a) the original velocity model, and (b) the updated model. [CR] `chap4/.imgv-yz0a,imgv-yz1a`

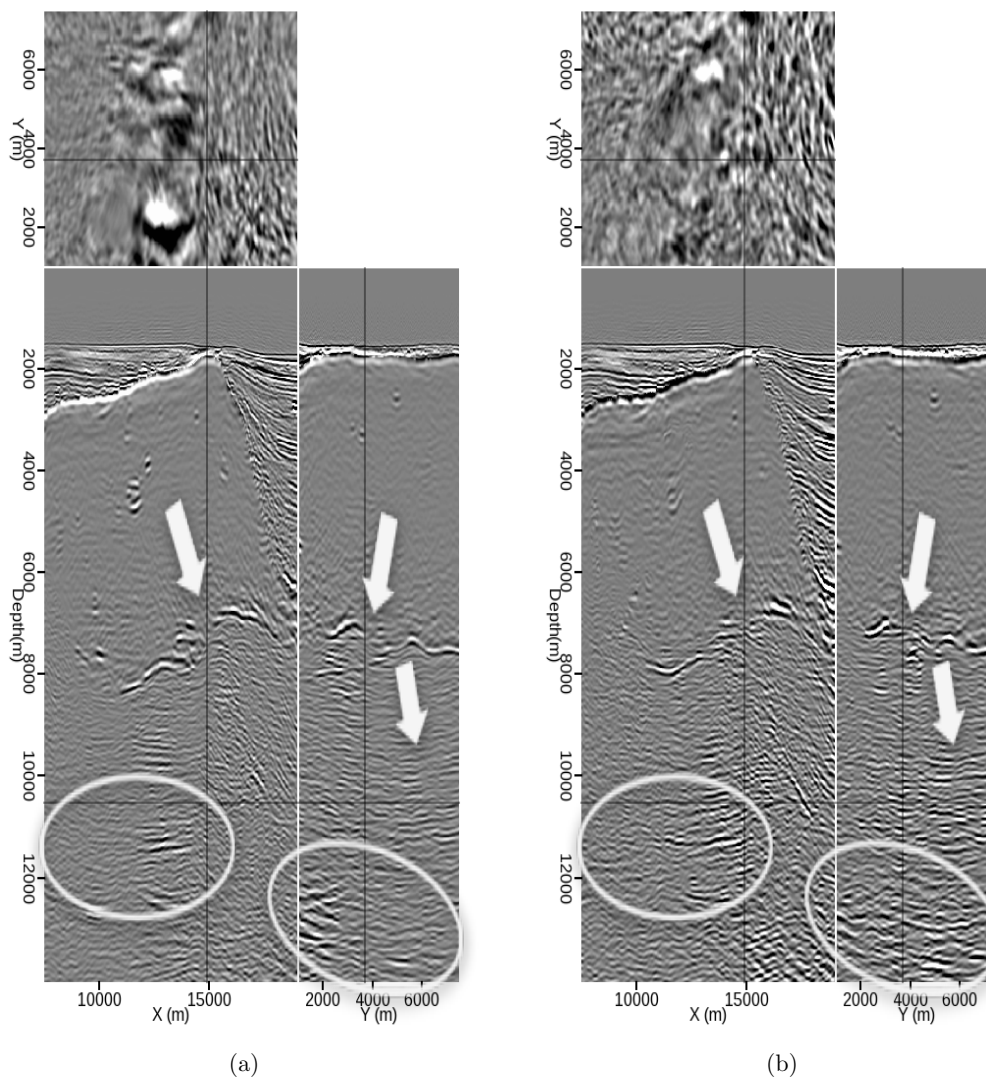


Figure 4.8: Same as Figure 4.7, but with areas of interest indicated. The deep subsalt reflectors and the base-salt reflector show particular improvement on the image generated with the new velocity model (b). [NR] chap4/. imga-yz0a,imga-yz1a

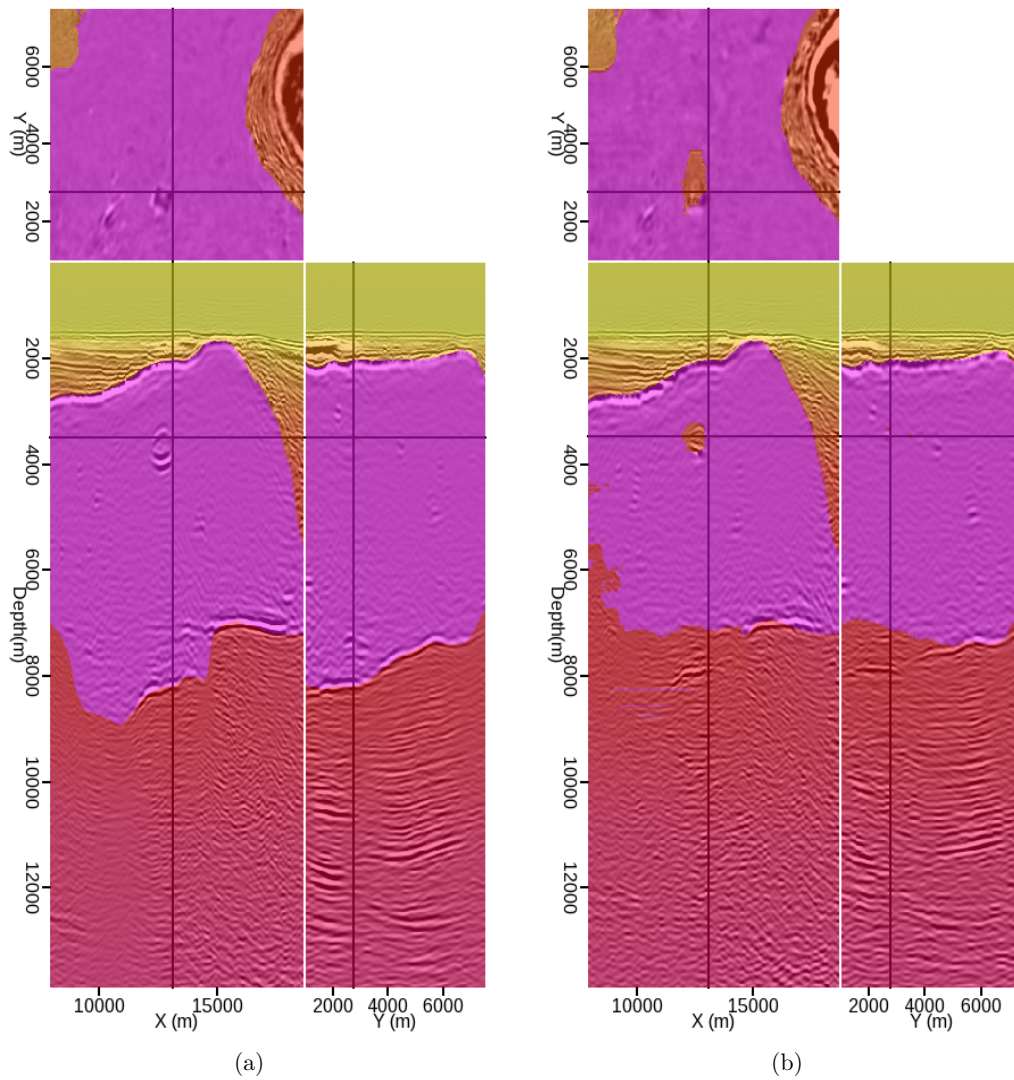


Figure 4.9: Images at a second location, obtained using (a) the original velocity model, and (b) the updated model. [CR] `chap4/. imgv-yz0b,imgv-yz1b`

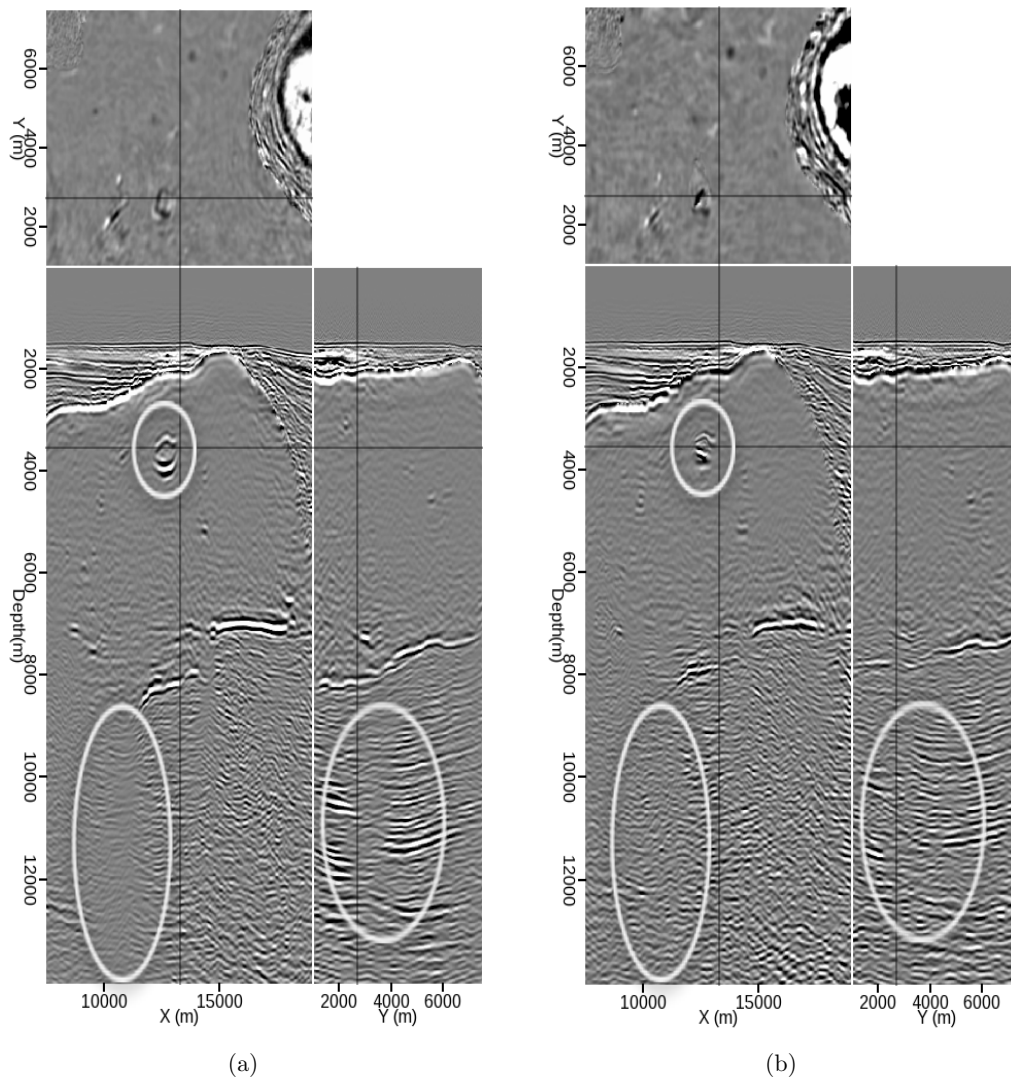


Figure 4.10: Same as Figure 4.9, but with areas of interest indicated. At this location, the subsalt reflectors show improved continuity and the salt inclusion is more accurately depicted on the image generated with the new velocity model (b). [NR]  
 chap4/. imga-yz0b,imga-yz1b

## ACKNOWLEDGMENTS

I thank Schlumberger Multicient for providing the wide-azimuth dataset used in this chapter. In addition, I am grateful to Yang Zhang for his assistance with imaging the full dataset.